MR performance in the presence of a radio frequency-penetrable positron emission tomography (PET) insert for simultaneous PET/MRI

Brian J. Lee [Student Member], **IEEE**,
Department of Mechanical Engineering, Stanford University, Stanford, CA, USA

Alexander M. Grant [Student Member], **IEEE**,
Department of Bioengineering, Stanford University, Stanford, CA, USA.

Chen-Ming Chang [Student Member], **IEEE**,
Department of Applied Physics, Stanford University, Stanford, CA, USA.

Ronald D. Watkins [Member], **IEEE**,
Department of Radiology, Stanford, CA, USA.

Gary H. Glover [Member], **IEEE**,
Department of Radiology, Neurosciences & Biophysics, Electrical Engineering & Psychology, Stanford, CA, USA

Craig S. Levin [Member], and **IEEE**
Departments of Bioengineering, Radiology, Electrical Engineering, and Physics, Stanford University, Stanford, CA, USA.

Abstract

Despite the great promise of integrated PET/MRI to add molecular information to anatomical and functional MR, its potential impact in medicine is diminished by a very high cost, limiting its dissemination. An "RF-penetrable" PET ring that can be inserted into any existing MR system has been developed to address this issue. Employing optical signal transmission along with battery power enables the PET ring insert to electrically float with respect to the MR system. Then, inter-modular gaps of the PET ring allow the RF transmit field from the standard built-in body coil to penetrate into the PET FOV with some attenuation that can be compensated for. MR performance, including RF noise, magnetic susceptibility, RF penetrability through and B_1 uniformity within the PET insert, and MR image quality, were analyzed with and without the PET ring present. The simulated and experimentally measured RF field attenuation factors with the PET ring present were −2.7 and −3.2 dB, respectively. The magnetic susceptibility effect (0.063 ppm) and noise emitted from the PET ring in the MR receive channel were insignificant. B_1 homogeneity of a spherical agar phantom within the PET ring FOV dropped by 8.4% and MR image SNR was reduced by 3.5 and 4.3 dB with the PET present for GRE and FSE, respectively. This study demonstrates, for the first time, an RF-penetrable PET insert comprising a full ring of operating detectors that achieves simultaneous PET/MR using the standard built-in body coil as the RF transmitter.

Keywords

PET; RF-penetrable; PET/MRI; MR compatible

I. Introduction

POSITRON emission tomography (PET) is a powerful molecular imaging modality that tracks the 3D biodistribution of radioactive biomarkers, allowing *in vivo* visualization and quantification of biological processes on the molecular level with picomolar sensitivity. A general drawback of PET is its lack of anatomic information, which poses a challenge for signal localization. The combination of high resolution morphology and functional information from MRI and molecular information from PET shows promise to be a powerful diagnostic tool and research platform [1]. Significant efforts have been made to achieve simultaneous PET/MR operation, which minimizes imaging time compared to performing separate PET and MR studies, improves modality co-registration, and provides concurrent, complementary functional, molecular and high resolution anatomical information with excellent soft tissue contrast for multi-parameter characterization of disease anatomy, physiology, biochemistry, and biology [2], [3], [4], [5].

There are different approaches to achieve simultaneous PET/MR acquisition. One method is to permanently integrate PET and MRI, which has many advantages including fixed alignment of two fields-of-view (FOV) [6], [7], [8], [9]. However, the clinical dissemination of such an integrated PET/MRI approach has been limited due to its high cost ($5 to $6 M, not counting required room renovations), restricting its availability. To solve this issue, research groups have developed PET rings that can be inserted and removed from existing MR systems [10], [11], [12], [13], [14], [15]. This PET insert approach could increase the prevalence of this dual-modality technique, since any existing MR center could in principle achieve simultaneous PET/MR.

The conventional PET insert designs for simultaneous brain PET/MR studies do not allow RF transmission from the standard MR body coil. Therefore, both the transmit (TX) as well as receive (RX) coils are required to be positioned inside the PET ring, either using a combined TX/RX birdcage [11], [12], [13], [14], [15], or separate TX (birdcage) and RX (array) coils [16]. To power the PET detectors inside the MR bore in these conventional approaches, carefully designed power supply system is necessary to avoid switching noise and/or magnetic susceptibility artifacts [11], [13], [14], [15]. However, long electrical cables, including the signal cables that relay PET information from the MR room to the PET data acquisition system and the power cables that supply DC voltage from the power supply to the PET system, may act as RF field antennas as well as pick up external electromagnetic noise from the surrounding environment. To mitigate these effects in conventional PET insert designs, RF chokes and filters are added to the electrical cables [15, 17].

An appealing alternative approach for simultaneous PET/MR imaging is an "RF-penetrable" PET insert, which can use the standard MR body coil for RF transmission. In this approach, the RF TX field penetrates into the PET FOV through small gaps between the detector modules of the PET insert and a uniform B_1 field is established inside the PET FOV. This

idea is facilitated by the use of optical signal transmission along with electrically floating battery power [18], [19], which enables the PET ring to electrically float with respect to the MR system. In previous work [20], only two PET detectors out of a total of 16 detectors required for the full-ring PET insert were inserted in the ring and preliminary PET detector performance along with some initial studies of RF penetrability were performed. In another study [21], the full-ring PET insert was inserted into an MR bore and reconstructed PET and MR images were analyzed. Building on the preliminary work, this paper is the first report of full MR performance studies with all 16 operating PET detector modules. As the system was scaled up to a full-ring PET insert for this work compared to only two prototype detectors from the previous work [20], the 14 additional scintillation detectors, electronic components, cables, fibers and batteries are potential strong sources of additional interference. Therefore, a more detailed analysis of MR performance (including the float/ground configuration, RF noise emission, B_0 map, RF- penetrability (B_1), and SNR analysis) without and with the full-ring PET insert present within the MR was warranted, and thus performed, and presented here for the first time.

II. Methods

A. Electrically Floating RF-Penetrable PET System

The full-ring prototype RF-penetrable PET insert is human head size, comprising 16 PET scintillation detector modules arranged in a 32 cm inner diameter ring with 1 mm inter-modular gaps and a 2.8 cm sensitive axial FOV. Each PET detector module (Fig. 1(a)) consists of a 2×4 tiling configuration of sub-units of arrays of 4×4 lutetium-yttrium orthosilicate (LYSO) scintillation crystals (3.2 mm x 3.2 mm x 20 mm) one-to-one coupled to silicon photomultiplier (SiPM) photodetector arrays (SensL, Ireland; 2008 version). The signals of the 128 SiPM pixels in each PET detector module are multiplexed to 16 output channels using a compressed sensing multiplexing circuit (Fig. 1(b)) [22], [23]. To electrically decouple ("float") the PET system from the MR system, the resulting electrical signals from the SiPM are converted into near infrared (NIR) optical signals using non-magnetic vertical cavity surface-emitting lasers (VCSELs) (Fig. 1(c)) and the system is powered by two sets of batteries that supply two distinct voltage levels: (1) Three high-voltage lead-acid-gel batteries (SLA1075, 12V, 7.5 Ah, Power Patrol) in series were fed to 16 linear voltage regulators (LT3013b, Linear Technology) to supply bias voltage of ~30V to each detector module via short shielded power cables, and (2) 16 low-voltage Lithium polymer batteries (DTXC1865, 7.4V, 5700 mAh, Duratrax) were each connected to a detector module, which contains a 5V voltage regulator (UA78M05, Texas Instruments) supplying the amplifier and VCSELs, via non-shielded battery cables [19], [20]. Short shielded power cables for high-voltage batteries were used to mitigate potential electromagnetic noise pick-up, as well as avoid the risk of electrical discharge on patients (Figs. 2 and 3) [24]. The scintillation crystals, photodetectors, electronic components and optical signal transmission components for each PET detector module are mounted on an FR-4 base printed circuit board and encapsulated in a 17.5 μm thick copper Faraday cage for shielding from the strong RF field emitted by the MRI system (Fig. 1(a)). The Faraday cage is a trapezoidal box with dimensions of 6.2 cm (short dimension) x 7.9 cm (long dimension) x 4.1 cm (height) x 21.4 cm (length). The thickness of the FR-4 bases were 0.8 mm (31 mil)

thick, except for the top plate which was 1.6 mm (62 mil) for structural rigidity. In addition, the top plate of the Faraday cage had small holes to dissipate heat out from the PET electronics. The NIR signals containing the scintillation information are then transmitted via 20 m optical fibers out of the cage through rectangular waveguides (cross-section: 1.25mm x 1.25 mm, depth: 8 cm) to conserve the shielding effectiveness (Fig. 1(a)). When the cross-sectional dimensions of the aperture (1.25 mm x 1.25 mm) are small relative to a half-wavelength of the RF frequency (~1.15 m at 127.8 MHz) and the depth of the waveguide is at least 5x longer than the aperture width, the energy propagating through the aperture significantly attenuates as an evanescent mode, thus, conserving the shielding effectiveness of the Faraday cage [25]. These fibers coming out from the waveguide are then transmitted out from inside the MRI bore to the data acquisition system residing in the adjacent control room. The environmental air conditioning system of the MRI was found to be adequate for thermal stability of the PET detectors during the simultaneous PET/MR studies, and no additional thermal stabilization was employed in this prototype insert.

In addition to facilitating the PET insert to electrically float with respect to the MR system, other advantages of employing electrically floating batteries with short shielded power cables for high-voltage DC power along with optical signal transmission for the PET system are: (1) reducing the risk of RF pickup through long shielded cables from within or outside of the magnet bore, (2) mitigating potential RF noise emission and (3) alleviating patient safety concerns (Fig. 2).

B. MRI Configuration

For inserting into a 3-Tesla MRI (MR750, GE Healthcare, 60-cm diameter bore), the PET insert prototype was placed onto the patient bed (Fig. 3). The isocenter of the PET sensitive FOV (scintillation crystal region) was axially and trans-axially aligned to the MR bore isocenter; therefore, since the PET crystals reside near to one end of the Faraday cages (see Fig. 1), the Faraday cages' axial center was axially shifted with respect to the MR system isocenter inside the MR bore. Fig. 3 shows the PET insert placed on the patient bed backwards to simplify setup for the studies reported here; however, for patient studies, this configuration will be flipped to facilitate patient access. In this study, the standard MR body coil was used as the TX/RX coil, which requires RF fields to penetrate both into and out of the PET ring, allowing a very sensitive study of the "RF-penetrability". In the MR experiments, a 17.5 cm diameter spherical MR agar phantom was used for imaging assessments. MR image acquisition parameters are listed in Table I.

C. Effect of PET Powering Configurations

To analyze the effect of PET powering configurations (Fig. 2) on MR performance, the detector ring was powered with (1) non-magnetic batteries electrically floating with respect to the MR system placed nearby using short (~1 m) or long (~7 m) shielded power cables for high-voltage supply, and (2) a floating or grounded switching power supply (GW INSTEK PST3202) placed far away in the adjacent control room and transmitting power through long shielded power cables with the electrical ground connected to the MR system ground. For the power supply with long power cable configuration, no baluns (common-mode chokes) and/or filters were applied to the power cables. 2D Fast spin echo (FSE) and 2D gradient

echo (GRE) images (Table I) of the agar phantom were acquired with auto pre-scan calibration and images were analyzed by measuring the signal-to-noise ratio (SNR) of the reconstructed images. The SNR was calculated using the below equation [26].

$$SNR = 0.655 \times \frac{mean\left(ROI_{phantom}\right)}{std\left(ROI_{Background}\right)} \quad 1$$

The mean signal in the center 75% ROI of the agar phantom and the standard deviation in a 5 cm^2 circular ROI of the background were analyzed over the center 8 axial slices of 31 total slices. The standard correction factor for Rician noise of 0.655 was used since magnitude images were used to assess the noise in the images [26].

D. Susceptibility Artifacts From the PET

Utilizing low- or non-magnetic PET components inside the MR bore to maintain the main magnetic field (B$_0$) homogeneity is imperative. The magnetic susceptibility of the PET insert system was analyzed by acquiring B$_0$ maps (phase measurement method [27]), which acquires two GRE sequence scans with different echo times (TE1/TE2/TR: 6.5/7.5/500 ms, Flip angle: 45°, Matrix: 64 × 64, Readout bandwidth: 1024 Hz/px), with and without the operating PET insert inside the MR system using the agar phantom. For quantitative analysis of the B$_0$ field map, the center 75% of the signal from the center 8 slices out of 20 total slices was selected as the region- of-interest for analysis and no shimming was applied.

E. Noise Emission From PET Electronics

PET electronics may emit noise that is detected by the RX coil. RF noise spectra were acquired with the PET insert powered (batteries connected) and off (batteries disconnected), with the MRI only receiving the background signals emitted from the PET insert within a bandwidth of ±62.5 kHz (typical receiver bandwidth for 2D GRE sequence, see Table I) centered around the Larmor frequency (127.8 MHz) without applying any RF pulse sequences. Only the RF pulse was turned off and the gradient field was turned on for examining any possible artifacts due to the gradient field (e.g. spike noise from metal contacts caused by Faraday cage vibration). The mean and standard deviation of the noise spectra were calculated. LYSO scintillation crystal natural background activity (~113 kevents/s) was used as the radioactive source for this study.

F. RF TX and RX Field Attenuation Through PET Ring

1) Electromagnetic Simulation: 3D electromagnetic simulations using XFdtd (REMCOM, USA), a finite-difference time-domain Maxwell's equation solver, were performed to numerically predict RF transmission through the inter-modular gaps of the PET ring. The RF field was generated from a simulated birdcage coil (60 cm diameter, 1 m length), representing the MR body coil, which surrounded a ring of 16 hollow 6 cm (short dimension) x 8 cm (long dimension) x 4 cm (height) x 20 cm (length) trapezoid copper boxes (32 cm inner diameter) with 1 mm inter-modular gaps, representing the PET ring. The simulated ring of Faraday cages was axially shifted by 7.5 cm to align the PET sensitive

FOV (scintillation crystal region) to the MR isocenter. The TX field attenuation was calculated by the following equation,

$$RF \text{ power attenuation} = 20 \log_{10}\left(\frac{RF \text{ field amplitude }_{with} \text{ PET}}{RF \text{ field amplitude }_{without} \text{ PET}}\right) \quad 2$$

where RF field amplitudes were averaged over the center 75% ROI of the PET FOV. The transmitted RF power maps of the simulated birdcage coil were acquired for each case with and without the Faraday cage ring present.

2) MR Experiment: In the auto pre-scan calibration of the MR studies, the RF transmit gain (TG) is usually adjusted to achieve the desired flip angle averaged over the sensitive region of the TX/RX coil(s). Therefore, the extra TG required with the PET present, compared to the "no PET" case, provides a measure of the TX field attenuation factor of the PET ring. For an alternate experimental measure of the TX field attenuation, the flip angle distribution was calculated through the double-angle B_1 mapping method [28], which measures the signal ratios between two scans with a flip angle α and 2α. By fixing the TG (not using auto pre-scan), the attenuation from the RF transmission was extracted after normalizing the RX attenuation. The B_1 field magnitude and homogeneity were calculated over the 8 center axial slices by the recommendations of the American Association of Physicists in Medicine [29],

$$Homogeneity(\%) = \left(1 - \frac{S_{max} - S_{min}}{S_{max} + S_{min}}\right) \times 100 \quad 3$$

where $S_{max/min}$ are the maximum/minimum values of the signal amplitude within the center 75% ROI of the agar phantom. The mean and standard deviation of center 8 slices were calculated and compared. B_1 maps and B_1 1D horizontal profiles were plotted.

To experimentally measure the RX field attenuation by the PET insert when the body coil is used as the RF TX/RX coil, the TG was varied by the auto pre-scan calibration to bring the flip angle to its nominal value. Then, the RX field attenuation of the RF signal from the phantom through the PET ring received by the standard body coil was calculated from the reduction in SNR of the MR images (for GRE, FSE and echo planar imaging (EPI) sequences—see Table I) over the center 8 axial slices of 20 total slices. In addition, quantitative SNR maps (using equation (1)) of GRE and FSE sequences were acquired; SNR calculation of EPI images was not analyzable due to significant ghosting artifacts (to be discussed).

To summarize the methods for measuring RF attenuation: comparing MR image SNR without and with the PET insert (with auto pre-scan turned on) enables an assessment of PET ring attenuation of the RF receive signal, whereas comparing B_1 maps (with auto pre-scan turned off) or TGs (with auto pre-scan turned on) without and with the PET insert allows a measure of PET ring attenuation of the RF transmit signal. For all results for the

"without PET" configuration in this work, the PET insert was not present inside the MR system.

III. Results

A. Effect of PET Powering Configurations

When the PET ring was powered using the electrically floating batteries with short power cables, the SNR of the reconstructed agar phantom was decreased by $-44.3 \pm 5.0\%$ (GRE) and $-40.0 \pm 4.6\%$ (FSE) as compared to the "no PET" case, but no significant MR image artifact was observed (Fig. 4). However, using the electrically floating batteries with long power cables decreased the SNR by an additional $-46.3 \pm 6.7\%$ (GRE) and $-32.9 \pm 6.7\%$ (FSE) with respect to that with short cables (Fig. 4). When the PET ring was powered using the grounded switching power supply with long power cables placed in the control room, in addition to a further SNR decrease of $-28.9 \pm 9.0\%$ (GRE) and $-34.2 \pm 7.4\%$ (FSE) with respect to electrically floating batteries with long power cables, a significant noise streak was observed in MR images due to the RF noise pickup in the cable (Fig. 4). Furthermore, the performance between the floating power supply and the grounded power supply did not show any significant difference.

B. Susceptibility Artifacts From the PET Insert

The B_0 field inhomogeneities observed between the cases without and with the PET insert present for the same pixel in each map were found to be smaller than 0.19 μT, which corresponds to 0.063 ppm in a 3T environment (Fig. 5). This indicates that the PET components placed inside the MRI bore have low magnetic susceptibility and any electrical current flowing in the PET electronics does not significantly distort the B_0 field in the useful imaging FOV.

C. Noise Emission From PET Electronics

The mean and standard deviation of the RF noise spectrum averaged over 14 timestamps with the PET ring powered on and off were 662.3 ± 355.0 a.u. and 687.9 ± 368.5 a.u., respectively (Fig. 6). Thus, no significant difference in RF noise spectra was observed, indicating that the 17.5 μm thickness copper Faraday cage sufficiently shields any emitted PET electronics noise within ± 62.5 kHz (typical receiver bandwidth for 2D GRE sequence, see Table I) of the Larmor frequency.

D. RF TX and RX Field Attenuation Through PET Ring

1) TX Field Attenuation: For the electromagnetic simulations, the RF field magnitude inside the PET ring was attenuated by ~2.7 dB (26.9%) compared to the case without the PET ring present (Fig. 7). The level of RF penetrability through the PET ring experimentally measured from the B_1 field mapping experiment is shown in Fig. 8 and Table II (top). The TG increase observed when the auto pre-scan was utilized to set TG is shown in Table II (bottom). Compared to the "no PET" case, the mean B_1 field amplitude was reduced by -3.2 ± 0.7 dB ($30.6 \pm 7.8\%$) and the homogeneity was degraded by $-8.4 \pm 6.8\%$ when the operating PET insert was present. This -3.2 ± 0.7 dB ($30.6 \pm 7.8\%$) TX attenuation factor was not significantly different (within error) of that derived from the TG increase seen with

auto pre-scan mode (−3.0 dB (29.2%)), as well as the −2.7 dB (26.9%) estimated from the electromagnetic simulations (Table II). In addition to the TX attenuation seen in Fig. 8, the B_1 map with an operating PET showed a checker-board pattern artifact, which will be further discussed in the next section.

2) RX Field Attenuation : Fig. 9 and Table III present the RF RX attenuation level using the standard MR body coil as both RF transmitter and receiver. EPI images were not analyzed for attenuation due to the significant ghosting artifacts observed with the PET ring present (Fig. 9). The image SNR reductions (RX field attenuation) compared to the "no PET" case with GRE and FSE sequences were −3.5 ± 0.9 dB and −4.3 ± 0.7 dB, respectively, and the image homogeneity drops were −6.6 ± 9.3% and −13.1 ± 11.5%, respectively. The FSE image had a larger homogeneity drop and SNR degradation compared to the no-PET case than for the GRE image.

IV. Discussion

We have demonstrated a proof-of-concept of an electrically floating RF-penetrable PET ring prototype that may be inserted into any existing MR system to achieve simultaneous PET/MR studies using the standard MR body coil as the TX coil. This work builds on preliminary studies for 2 of 16 detectors present in the PET ring [20] and, for the first time, reports on a more thorough study of RF-penetrability (float/ground configuration and B_1 map) and MR performance (RF noise spectrum, B_0 map, SNR image analyses) with the full set of 16 PET detectors, electronics and full data acquisition system operating simultaneously with the MR system. The PET performance of the full ring of 16 detectors [30], and the preliminary simultaneous PET/MR imaging results of the full ring of 16 PET detectors [21], have been studied earlier.

A. Standard MR Body Coil as an RF Transmitter and Multichannel Coil as an RF Receiver

Although using the standard MR body coil as an RX coil is not desired in brain imaging, in this study the body coil was used as a TX/RX coil to enable a very sensitive study of the "RF-penetrability" concept as the RF transmit and receive fields must penetrate both into (Figs. 7 and 8, Table II) and out of (Fig. 9 and Table III) the PET ring. For better MR image SNR, an RX coil should be placed inside the PET ring, close to the body; however, unlike conventional PET insert designs, the RF-penetrable design does not require a TX coil (in addition to an RX coil; e.g. TX/RX birdcage coil) inside the PET ring, simplifying the insertion of the PET ring into an existing MR system in order to achieve simultaneous PET/MR. Other potential benefits of using the standard MR body coil as the transmitter compared to a re-engineered smaller diameter TX coil inside the PET insert [10], [11], [12], [13], [14], [15] are (1) better TX field homogeneity, and (2) less material inside the PET ring for lower 511 keV photon attenuation.

Another advantage of using the standard MR body coil as an RF transmitter is that a high performance RX-only multichannel array coil can be used inside the PET ring. In MR-only brain studies, most high performance brain imaging is performed using the standard MR body coil for RF TX and a multi-channel RX coil (e.g. phased-array loops) for RF RX [31]. The conventional PET insert design for simultaneous PET/MR systems employs a TX/RX

birdcage coil inside the PET ring [10], [11], [12], [13], [14], [15], since their PET designs are not RF penetrable. However, the RF-penetrable PET ring allows RF transmission from the standard MR body coil, thus, a multi-channel RX coil can be placed inside the PET ring to achieve higher SNR MR images, faster acquisition speed and parallel imaging abilities compared to birdcage coils [32], [33]. This RX coil inside the PET insert will slightly attenuate the detected PET annihilation photon flux; however, with careful PET-compatible design using low-density materials in the PET FOV, the impact on PET performance should be negligible [16], [34], [35]. This custom multi-channel RX coil is the subject of another study [36, 16].

B. Potential to Scale Up to Larger PET System Geometries

Although we have demonstrated the RF-penetrable concept with a 32 cm diameter and 3 cm axial FOV (scintillation crystal region) ring, the idea can be scaled to larger detector volumes (e.g. 32 cm diameter/16 cm axial FOV for the brain or a 60 cm diameter/25 cm axial FOV for whole-body). When scaled to a longer axial FOV, the detector configuration and front-end electronics will have to be re-designed for higher compactness and more readout channels in a restricted space. From an MR perspective, the magnetic susceptibility, PET electronics shielding and RF-penetrability are primary concerns for scaling up the PET insert design to larger volumes. As non-magnetic PET detector materials (scintillation crystals and photodetectors) are now widely available, there are less concern about magnetic susceptibility. Further consideration is needed regarding shielding the PET electronics noise, as introducing digital electronics, additional integrated circuits, or FPGAs inside the MR bore could potentially generate MR- disturbing frequencies. Appropriate shielding and careful layout of the electronics should limit emission of unwanted noise from the PET ring. If the Faraday cage must be lengthened due to the increased number of components inside a detector module, then its radial dimension (cage height) should be reduced and/or the gap between the adjacent detector module cages should be slightly widened beyond the 1 mm employed in this work to maintain sufficient RF-penetrability. Widening the gap between the Faraday cages does not necessarily require the gap between the scintillation crystals to widen as well. Therefore, the RF-penetrability can be increased while maintaining the PET system photon sensitivity (Fig. 10).

C. Powering Mechanisms

In Fig. 4, we observed that floating batteries with short power cables are preferable to achieve low noise MR images. Powering with batteries requires low power consumption PET detectors and readout electronics and a daily recharge. However, the battery powering configuration is easier to implement compared to the standard power supply configuration. In the case of high power consumption system, regulated power supplies could be a better option. When using a power supply, the results in Fig. 4 showed that the "switching" power supplies, regardless of the powering configuration (electrically floating or grounded), using long shielded power cables and no RF traps could generate noise from high frequency switches and RF induction on the cables. There are methods to avoid this switching noise or RF induced noise. Several stages of baluns and filters can be added to the long power cables to mitigate common-mode RF power on the cable and switching noise from the power supply [37], [38]. A linear power supply, which does not employ switching currents, with

the addition of multiple filtering stages and traps can mitigate these problems [39], [40]. However, these methods are beyond the scope of this study since, due to low power requirements, electrically floating batteries were found to be sufficient.

D. Faraday Cage and Shielding Effectiveness

The main function of the Faraday cage is to safely shield the PET electronics from the intense electromagnetic fields of MR without producing artifacts and vice versa. If the shielding for the PET electronic noise were not sufficient, discrete frequencies or a broader baseline noise would be observed in the RX spectrum. However, in Fig. 6, both spectra were broadband white noise with insignificantly different baseline noise level and no discrete frequencies were observed within the measured receiver bandwidth (±62.5 kHz) around the Larmor frequency. Other important features that facilitated this negligible RF pick-up was that the PET detectors directly convert their analog output electrical signal into an optical signal within a short electrical path inside each shielded module, and no digital signal processing is performed inside the MR bore.

E. RF-Penetrability

Although the RF TX field penetrates through the PET ring, the RF field attenuates. This RF penetrability was analyzed in simulation and experimentally and an insignificant discrepancy between the corresponding TX field attenuation factors was observed (-2.7 dB (26.9%) (Fig. 7) and -3.2 ± 0.7 dB (30.6 ± 7.8) (Fig. 8, Table II), respectively). The higher average TX field attenuation in the experiment may be a result from not including the extra components placed nearby the PET ring in the simulation; these extra features, such as power cables and low voltage batteries (Fig. 3), were excluded from the simulation due to the complexity of accurately simulating them. The relatively large error (0.7 dB) of TX field attenuation may result from the non-uniform axial B_1 field magnitude. The axial B_1 field map slice closer to the outer edge of the PET ring has higher B_1 field and the slice inside the PET ring has lower B_1 field, which increases the deviation of the B_1 field magnitude over multiples slices.

Currently, TX field attenuates by -3.2 dB (Fig. 8 and Table II (Top)) in the experiment, but this attenuation is compensated by the auto pre-scan feature, which increases the TG by 3.0 dB (Table II (Bottom)) [41]. This increase in TG leads to an acceptable increase in specific absorption rate (SAR) in body regions outside the PET insert [42]. Even though RF field attenuation can be compensated for by increasing TG, within an acceptable range of SAR increase, further improvements in RF penetrability of the PET insert are desirable to avoid raising TG too high during MR operation, in addition to avoiding SAR increases. SAR reported by the scanner is typically calculated by the subject weight/body location and the RF power deposition estimated from TG. However, the TG in our case is increased to compensate for the losses induced by the PET ring, resulting in an inaccurate SAR measurement. Therefore, only theoretical SAR studies and no experimental data was investigated in this work.

Reduction in RF attenuation by the insert is possible with minor revisions to the PET ring design. The ring of PET Faraday cages functionally resembles a series of capacitors, since

the side plates of two adjacent modules effectively form a capacitor. When the inter-modular gap between adjacent Faraday cages increases (ideally without changing the inter-module scintillation crystal spacing) or its height or length (radial or axial dimension) decrease, the capacitive impedance increases, resulting in less power dissipation, hence less RF power attenuation. This will reduce the required TG increase, reducing the SAR in the regions that are unshielded by the PET ring (e.g. torso). With the current prototype, even with the +3.0 dB TG used in this study, the SAR in the head region inside the PET insert is approximately the same as without the PET insert and the SAR in the body region outside the PET insert is under the upper limit allowed (whole-body: 4 W/kg/15 minute exposure averaged) [42]. However, if lower SAR is desired, besides the modifications stated above, an alternate approach could be lowering the bandwidth of the RF pulse, which would result in an increased pulse duration and longer scanning time [43].

F. MR Images and B_1 Field Map Characteristics

In Table III, the FSE image had a larger homogeneity drop and SNR degradation compared to the no-PET case than for the GRE image. During the FSE sequence, which has multiple RF pulses, any RF field inhomogeneity or attenuation from the PET insert causes errors to aggregate during an acquisition, whereas the GRE sequence only has an initial RF excitation for acquisition. This worse degradation in FSE images could be improved by avoiding the minor errors caused by the RF field inhomogeneity and/or attenuation. Higher RF penetrability and a custom RX coil inside the PET ring will potentially eliminate the FSE error source that we have observed with the standard MR body coil as RX.

EPI images showed worse image quality in several aspects compared to GRE and FSE, and these artifacts made the EPI images non-analyzable for this work as well as unacceptable for clinical use. In addition to the SNR drop due to the RX sensitivity loss, EPI images showed susceptibility-induced air bubbles and suffered from ghosting artifact (Fig. 9). The EPI sequence incorporates extreme gradient slew rates and duty cycles and suffers from susceptibility variations. Due to these reasons, the susceptibility variation between the air bubbles and the agar materials in the phantom appear more significantly in the images regardless of the PET being present inside the MR bore. When the PET insert is present, the gradient fields of the EPI sequence induce eddy currents, and the secondary magnetic fields contribute to the ghosting artifacts.

In addition to the ghosting artifact in the EPI images, the B_1 field maps with an operating PET also suffered from checker-board pattern artifacts (Fig. 8(a)). The B_1 mapping sequence was acquired with a standard double-angle method, which utilizes relatively high performance gradients for a single shot acquisition [28]. The extensive gradient slew rate induces eddy currents on conductive Faraday cages, which could lead to cage vibration. This vibration results in periodic contact between adjacent cages and leads to large-amplitude noise pulses ("spike noise"), which appear at random parts of k- space during the readout. This defective data point in the k- space shows up as diagonal lines throughout the reconstructed image [44].

As EPI images are crucial for neuroimaging applications, we have investigated ways to mitigate these artifacts. There has been extensive study on correcting for the susceptibility-

related field variation artifacts [45]. These methods can be used to resolve the air bubble artifact in the EPI images. Furthermore, there have been approaches to mitigate the gradient field-induced eddy currents by reducing the thickness of the copper Faraday cage, disrupting the current loops with patterns, and trying different materials while preserving the shielding effectiveness [46, 47].

V. Conclusion

We have shown for the first time from experiments and simulations that the RF TX field from an external MR body coil in an MR system can penetrate a complete ring of electrically floating and operating PET detectors through inter-modular gaps. The condition of electrically floating (with respect to the MR system) was enabled by using electro-optical signal transmission technology and the use of electrically floating batteries for power. The RF TX field attenuation (~35%) through the PET ring can be compensated for by increasing the TG by the same amount, resulting in an acceptable TX power increase. Although the MR body coil was used as the RF transmitter and receiver in this work to enable a sensitive study of RF penetration both into and out of the PET insert, for better MR performance we plan to integrate a high performance RX- only coil inside the PET ring [36].

The results show great promise for the RF-penetrable PET insert to enable an existing MR system to achieve simultaneous PET/MRI without modifying the MRI system, much like high-end RF coils that can be inserted and removed. This is a much less expensive approach to achieve simultaneous PET/MR compared to the purchase and installation of a new integrated PET/MR system (where the PET and MR systems are inseparable), potentially making it easier to more widely adopt and disseminate PET/MR.

Acknowledgment

References

[1]. Wehrl HF, Sauter AW, Divine MR, and Pichler BJ, "Combined PET/MR: A Technology Becomes Mature," J Nucl Med, vol. 56, no. 2, pp. 165–168, 2015 [PubMed: 25593114]

[2]. Pichler BJ, Judenhofer MS, and Pfannenberg C, "Multimodal Imaging Approaches: PET/CT and PET/MRI," in Handb Exp Pharmacol, vol. 185, pp. 109–132, 2008

[3]. Delso G, ter Voert E, de Galiza Barbosa F, and Veit-Haibach P, "Pitfalls and Limitations in Simultaneous PET/MRI," Semin Nucl Med, vol. 45, no. 6, pp. 552–559, 2015 [PubMed: 26522396]

[4]. Disselhorst JA, Bezrukov I, Kolb A, Parl C, and Pichler BJ, "Principles of PET/MR Imaging," J Nucl Med, vol. 55 (supplement 2), pp. 2S–10S, 2014 [PubMed: 24819419]

[5]. Nensa F, Beiderwellen K, Heusch P, and Wetter A, "Clinical applications of PET/MRI: current status and future perspectives," Diagn Interv Radiol, vol. 20, no. 5, pp. 438–447, 2014 [PubMed: 25010371]

[6]. Delso G, Furst S, Jakoby B, Ladebeck R, Ganter C, Nekolla SG, Schwaiger M, and Ziegler SI, "Performance measurements of the Siemens mMR integrated whole-body PET/MR scanner," J Nucl Med, vol. 52, no. 12, pp. 1914–22, 2011 [PubMed: 22080447]

[7]. Zaidi H, Ojha N, Morich M, Griesmer J, Hu Z, Maniawski P, Ratib O, Izquierdo-Garcia D, Fayad ZA, and Sha L, "Design and performance evaluation of a whole-body Ingenuity TF PET-MRI system," Phys Med Biol, vol. 56, no. 10, pp. 3091–106, 2011 [PubMed: 21508443]

[8]. Levin CS, Maramraju SH, Khalighi MM, Deller TW, Delso G, and Jansen F, "Design Features and Mutual Compatibility Studies of the Time-of-Flight PET Capable GE SIGNA PET/MR System," IEEE Trans Med Imaging, vol. 35, no. 8, pp. 1907–1914, 2016 [PubMed: 26978664]

[9]. Grant AM, Deller TW, Khalighi MM, Maramraju SH, Delso G, and Levin CS, "NEMA NU 2–2012 performance studies for the SiPM- based ToF-PET component of the GE SIGNA PET/MR system," Med Phys, vol. 43, no. 5, pp. 2334–2343, 2016 [PubMed: 27147345]

[10]. Kolb A, Wehrl H, Hofmann M, Judenhofer M, Eriksson L, Lade- beck R, Lichy M, Byars L, Michel C, Schlemmer HP, Schmand M, Claussen CD, Sossi V, and Pichler BJ, "Technical performance evaluation of a human brain PET/MRI system," Eur Radiol, vol. 22, no. 8, pp. 1776–1788, 2012 [PubMed: 22752524]

[11]. Jung JH, Choi Y, Hong KJ, Kang J, Hu W, Lim HK, Huh Y, Kim S, Jung J, and Kim KB, "Development of brain PET using GAPD arrays," Med Phys, vol. 39, no. 3, pp. 1227–1233, 2016

[12]. Peng BJ, Walton JH, Cherry SR, and Willig-Onwuachi J, "Studies of the interactions of an MRI system with the shielding in a combined PET/MRI scanner," Phys Med Biol, vol. 55, no. 1, pp. 265–280, 2010 [PubMed: 20009193]

[13]. Nishikido F, Obata T, Shimizu K, Suga M, Inadama N, Tachibana A, Yoshida E, Ito H, and Yamaya T, "Feasibility of a brain-dedicated PET- MRI system using four-layer DOI detectors integrated with an RF head coil," Nucl Instrum Methods Phys Res A, vol. 756, pp. 6–13, 2014

[14]. Wehner J, Weissler B, Duppenbecker PM, Gebhardt P, Gold-schmidt B, Schug D, Kiessling F, and Schulz V, "MR-compatibility assessment of the first preclinical PET-MRI insert equipped with digital silicon photomutlipliers," Phys Med Biol, vol 60, no. 6, 2231–2255, 2015 [PubMed: 25684065]

[15]. Weissler B, Gebhardt P, Duppenbecker PM, Wehner J, Schug D, Lerche CW, Goldschmidt B, Salomon A, Verel I, Heijman E, Perkuhn M, Heberling D, Botnar RM, Kiessling F, and Schulz V, "A digitla preclinical PET/MRI insert and initial results,"IEEE Trans Med Imaging, vol 34, no. 11, pp. 2258–2270, 2015 [PubMed: 25935031]

[16]. Sander CY, Keil B, Chonde DB, Rosen BR, Catana C, and Wald LL, "A 31-Channel MR Brain Array Coil Compatible with Positron Emission Tomography," Magn Reson Med, vol. 73, no. 6, pp. 2363–2375, 2015 [PubMed: 25046699]

[17]. Harrison WH, Arakawa M, and McCarten BM, "RF coil coupling for MRI with tuned RF rejection circuit using coax shield choke," U.S. Patent 4682125 A, Jul. 21, 1987

[18]. Bieniosek MF, Olcott PD, and Levin CS, "Readout Strategy of an Electro-optical Coupled PET Detector for Time-of-Flight PET/MRI," Phys Med Biol, vol. 58, no. 20, pp. 7227–7238, 2013 [PubMed: 24061218]

[19]. Olcott PD, Peng H, and Levin CS, "Novel Electro-Optical Coupling Technique for Magnetic Resonance-Compatible Positron Emission Tomography Detectors," Mol Imaging, vol. 8, no. 2, pp. 74–86, 2009 [PubMed: 19397853]

[20]. Olcott PD, Kim E, Hong KJ, Lee BJ, Grant AM, Chang CM, Glover G, and Levin CS, "Prototype positron emission tomography insert with electro-optical signal transmission for simultaneous operation with MRI," Phys Med Biol, vol. 60, no. 9, pp. 3459, 2015 [PubMed: 25856511]

[21]. Grant AM, Lee BJ, Chang CM, and Levin CS, "Simultaneous PET/MR imaging with a radio frequency-penetrable PET insert," Med Phys, vol. 44, no. 1, pp. 112–120, 2017 [PubMed: 28102949]

[22]. Olcott PD, Chinn G, and Levin CS, "Compressed sensing for the multiplexing of PET detectors," in IEEE NSS/MIC, Valencia, 2011, pp. 3224–3226.

[23]. Chang CM, Grant AM, Lee BJ, Kim E, Hong KJ, and Levin CS, "Performance characterization of compressed sensing positron emission tomography detectors and data acquisition system," Phys Med Biol, vol. 60, no. 16, pp. 6407, 2015 [PubMed: 26237671]

[24]. Dempsey MF, Condon B, and Hadley DM, "Investigation of the factors responsible for burns during MRI," J Magn Reson Imaging, vol 13, no. 4, pp. 627–631. 2001 [PubMed: 11276109]

[25]. Ott H, Electromagnetic Compatibility Engineering, John Wiley & Sons, New York, 2009.

[26]. Henkelman RM, "Measurement of signal intensities in the presence of noise in MR images," Med Phys, vol. 12, no. 2, pp. 232–233, 1985 [PubMed: 4000083]

[27]. Shmueli K, de Zwart JA, van Gelderen P, Li TQ, Dodd SJ, and Duyn JH, "Magnetic Susceptibility Mapping of Brain Tissue In Vivo Using MRI Phase Data," Magn Reson Med, vol. 62, no. 6, pp. 1510–1522, 2009 [PubMed: 19859937]

[28]. Insko EK and Bolinger L. "Mapping of the Radiofrequency Field," J Magn Reson, Series A, Vol. 103, no. 1, pp. 82–85, 1993

[29]. Price RR, Axel L, Morgan T, Newman R, Perman W, Schneiders N, Selikson M, Wood M, and Thomas SR, "Quality assurance methods and phantoms for magnetic resonance imaging: report of AAPM nuclear magnetic resonance Task Group No. 1," Med Phys, vol 17, no. 2, pp. 287–95, 1990 [PubMed: 2333055]

[30]. Chang CM, Grant AM, Lee BJ, and Levin CS, "Preliminary PET performance evaluation of an RF field-penetrable brain-sized PET insert for simultaneous PET/MR imaging," J Nucl Med, vol 56, pp. 99, 2015

[31]. Welker KM, Tsuruda JS, Hadley JR, and Hayes CE, "Radio-frequency Coil Selection for MR Imaging of the Brain and Skull Base," Radiology, vol. 221, no. 1, pp. 11–25, 2001 [PubMed: 11568316]

[32]. Chang G, Wiggins GC, Xia D, Lattanzi R, Madelin G, Raya JG, Finnerty M, Fujita H, Recht MP, and Regatte RR, "Comparison of a 28 Channel-Receive Array Coil and Quadrature Volume Coil for Morphologic Imaging and T2 Mapping of Knee Cartilage at 7 Tesla," J Magn Reson Imaging, vol. 35, no. 2, pp. 441–448, 2012 [PubMed: 22095723]

[33]. Porter JR, Wright SM, and Reykowski A, "A 16-element phased- array head coil," Magn Res Med, vol. 40, no. 2, pp. 272–279, 1998

[34]. Dregely I, Lanz T, Metz S, Mueller MF, Kuschan M, Nimbalkar M, Bundschuh RA, Ziegler SI, Haase A, Nekolla SG, and Schwaiger M, "A 16-channel MR coil for simultaneous PET/MR imaging in breast cancer," Eur Radiol, vol. 25, no. 4, pp. 1154–1161, 2015 [PubMed: 25287263]

[35]. Nelson G and Reilly D, "Gamma-ray interactions with matter," in Passive Nondestructive Analysis of Nuclear Materials, Los Alamos National Laboratory, NUREG/CR-5550, LAUR-90–732 pp. 27–42, 1991

[36]. Lee BJ, Grant AM, Chang CM, Watkins R, and Levin CS, "MR performance evaluation of an RF-penetrable PET insert with integrated RF receive coil for simultaneous PET/MRI," J Nucl Med, vol. 56, pp. 1854–1854, 2015

[37]. Yang X, Zheng T, and Fujita H, "T/R switches, baluns, and detuning elements in MRI RF coils," in ISMRM, unpublished, 2006

[38]. Peterson DM, Beck BL, Duensing GR, and Fitzsimmons JR, "Common mode signal rejection methods for MRI: Reduction of cable shield currents for high static magnetic field systems," Concepts Magn Reson B, vol. 19B, no. 1, pp. 1–8, 2003

[39]. Kimmel WD and Gerke DD, Electromagnetic compatibility in medical equipment: a guide for designers and installers, Taylor & Francis; 1995.

[40]. Geetha S, Satheesh Kumar KK, Rao CRK, Vijayan M, and Trivedi DC. "EMI shielding: Methods and materials—A review," J Appl Polym Sci, vol. 112, no. 4, pp. 2073–2086, 2009

[41]. Lee BJ, et al., "RF-transmissive PET detector insert for simultaneous PET/MRI," 2014 IEEE NSS/MIC, Seattle, WA, 2014, pp. 1–3.

[42]. U.S. Department of Health and Human Services, Food and Drug Administration, Center for Devices and Radiological Health, "Submission Of Premarket Notifications for Magnetic Resonance Diagnostic Devices," in Guidance for Industry and Food and Drug Administration Staff, Nov. 18, 2016.

[43]. Wu X, Akgün C, Vaughan JT, Andersen P, Strupp J, U urbil K, and Van de Moortele PF, "Adapted RF Pulse Design for SAR Reduction in Parallel Excitation with Experimental Verification at 9.4 Tesla," J Magn Reson, vol. 205, no. 1, pp. 161–170, 2010 [PubMed: 20556882]

[44]. Kao YH and MacFall JR, "Correction of MR k-space data corrupted by spike noise," IEEE Trans Med Imaging, vol. 19, no. 7, pp. 671–680, 2000 [PubMed: 11055782]

[45]. Liu G and Ogawa S, "EPI image reconstruction with correction of distortion and signal losses," J Magn Reson Imaging, vol 24, pp. 683–689, 2006 [PubMed: 16892198]

[46]. Lee BJ, Watkins RD, Chang CM, and Levin CS, "Low eddy current RF shielding enclosure designs for 3T MR applications," Magn Reson Med, vol. 79, pp. 1745–1752, 2018 [PubMed: 28585334]

[47]. Gross-Weege N, Dey T, Gebhardt P, Schug D, Weissler B, Schulz V, "Characterization methods for comprehensive evaluations of shielding materials used in an MRI," Med Phys, Accepted Author Manuscript. doi: 10L:1002/mp.12762
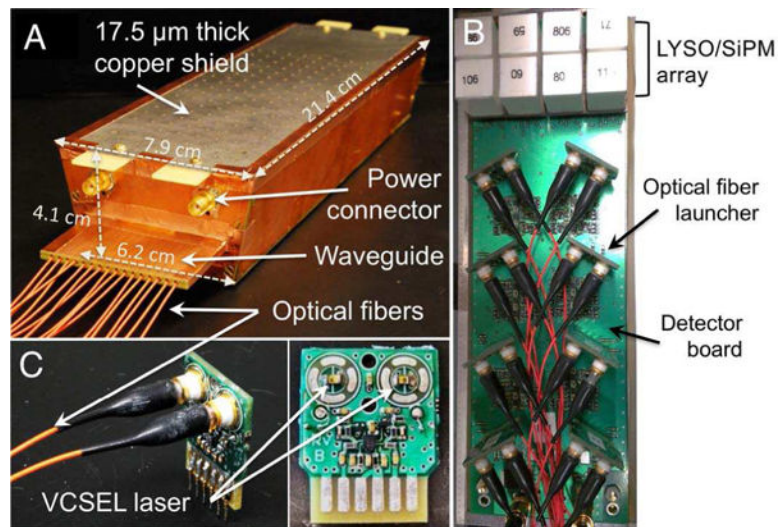
Fig. 1.

(A) PET detector Faraday cage (bottom segment 6.2 cm, top segment 7.9 cm, height 4.1 cm, length 21.4 cm) with optical fibers exiting the end through a waveguide. (B) Electro-optical PET detector module comprising 128 LYSO scintillation crystal elements each coupled one-toone to SiPM pixels (the crystals span a 3 cm x 6 cm area); "compressed sensing" multiplexing circuit that multiplexes the 128 SiPM signals to 16 readout channels; (C) Optical transmitter boards each containing two nonmagnetic VCSELs.
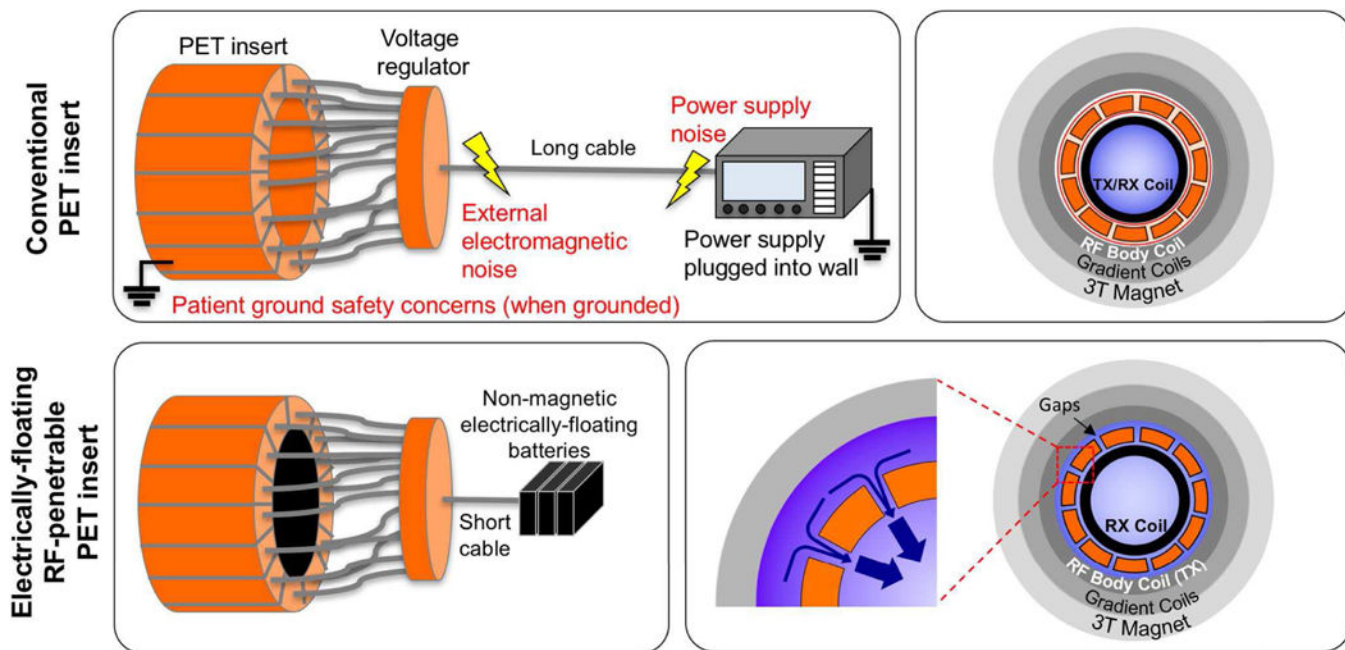
Fig. 2.
Conceptual comparison between (**TOP**) the conventional and (**BOTTOM**) electrically floating RF-penetrable PET system configurations for simultaneous PET/MR. The electrically floating feature of the latter design, enabled by optical signal transmission and electrically floating batteries, along with short power cables minimizes electromagnetic pick-up noise and promotes a patient-safe environment. In the latter configuration, the RF field from the standard body coil penetrates through small gaps between the PET detector modules to create a uniform B_1 field inside the sensitive field-of-view.
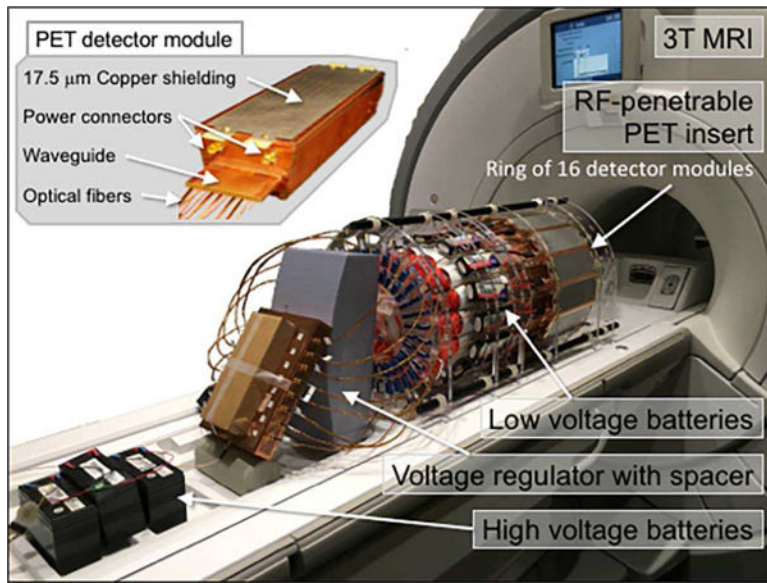
Fig. 3.
RF-penetrable PET ring prototype was inserted into a 3-T MRI. The 16 PET detector modules were populated with detectors/electronics, electro- optical signal transmission components, and powered by electrically floating non-magnetic batteries.
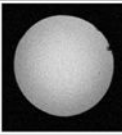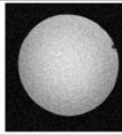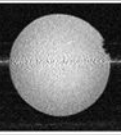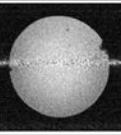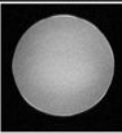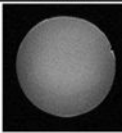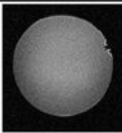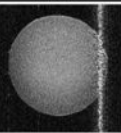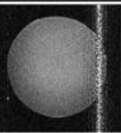
	No PET	With PET, Batteries in MR (short cables)	With PET, Batteries in control room (long cables)	With PET, *Floating* power supply in control room (long cables)	With PET, *Grounded* power supply in control room (long cables)
GRE					
SNR	50.8±1.9	28.3±1.5	15.2±0.9	11.8±0.8	10.8±1.0
FSE					
SNR	37.0±1.1	22.2±1.2	14.9±0.8	9.1±0.7	9.8±0.7

Fig. 4.
SNR comparison of the MR image with PET powered with electrically floating batteries using short (~1 m) and long (~7 m) cables, and a floating/grounded power supply plugged into mains power using ~7 m length cable. Center slices are shown. The air bubble shown in different positions of the phantom is due to repositioning of the phantom between different scan configurations.
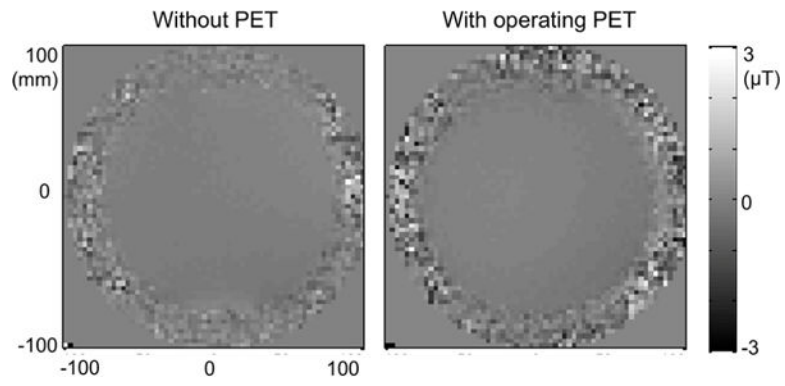
Fig. 5.

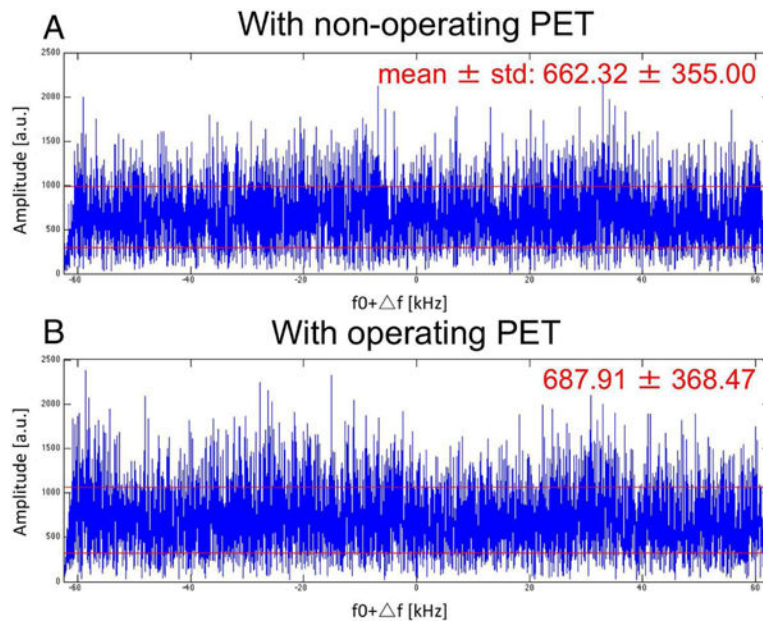B_0 field maps without and with operating PET present. Center slices are shown.

Fig. 6.
RF noise spectra with the PET ring (A) not operating (unpowered) and (B) operating. Red lines indicate ±1 standard deviation from mean.
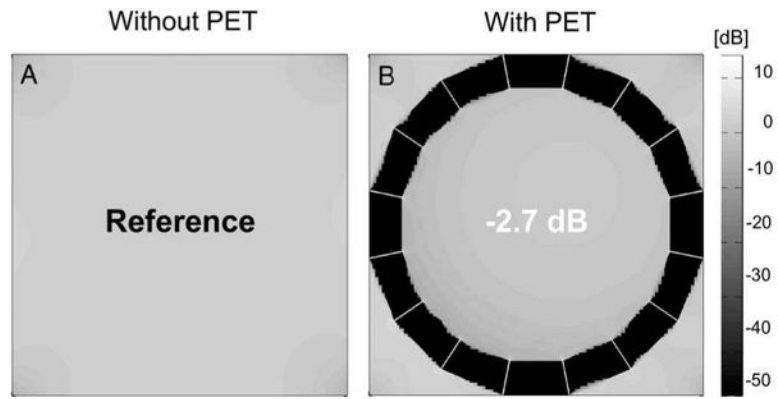
Fig. 7.
3D electromagnetic simulations of B_1 field distribution magnitudes (A) without and (B) with PET. The RF field lines enter through the 1 mm gaps between PET detector modules but do not penetrate the Faraday cages surrounding each module. Center slices are shown.
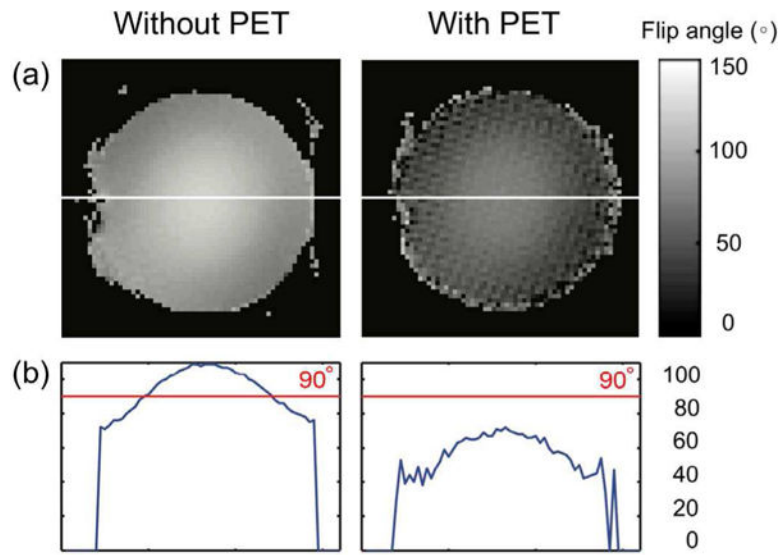
Fig. 8.
(a) B_1 field map and (b) a 1D B_1 horizontal profile without and with the PET ring, showing RF TX field attenuation. Center slices are shown.
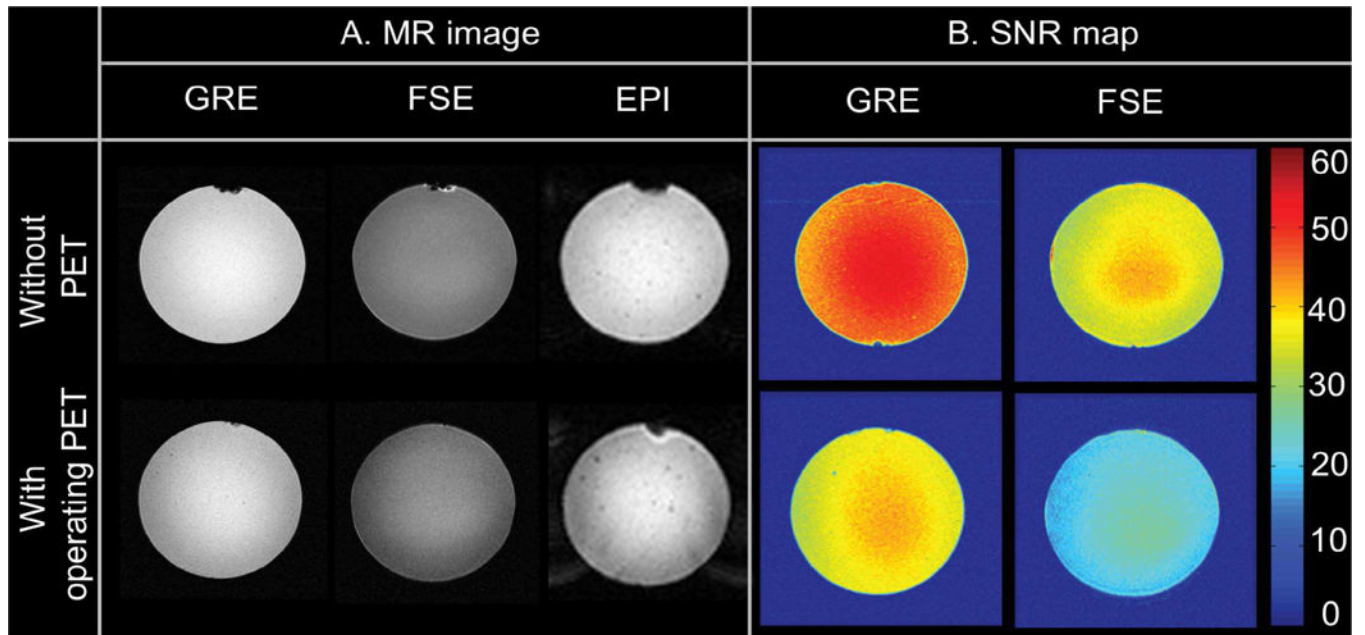
Fig. 9.
RX field attenuation was measured through (A) MR images and (B) SNR maps of GRE and FSE sequences. SNR maps of the EPI sequence were not calculated due to the ghosting artifact. Center slices are shown.
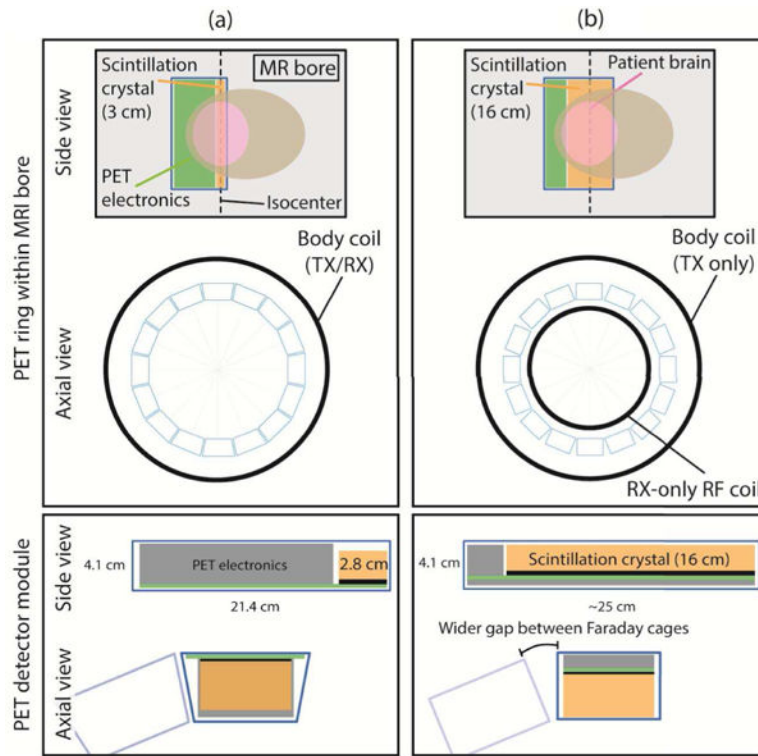
Fig. 10.
Comparison between (a) the RF-penetrability setup and (b) the new prototype currently under construction.

TABLE I

MR Pulse Sequence Parameters

Sequence	2D GRE	2D FSE	2D EPI
TR (ms)	3000	500	2000
TE (ms)	71	5	30
Voxel(mm³)	$0.86 \times 0.86 \times 4.00$	$0.86 \times 0.86 \times 4.00$	$3.44 \times 3.44 \times 4.00$
Matrix	256×256	256×256	64×64
Readoutbandwidth(Hz/Px)	244.141	122.109	7812.5
Flip angle	90	90	90
Numberof slices	31	31	31

TABLE II

B$_1$ ғɪᴇʟᴅ Mᴀᴘ ᴀɴᴅ TG Rᴇsᴜʟᴛs Usɪɴɢ Bᴏᴅʏ Cᴏɪʟ ᴀs TX/RX Cᴏɪʟ

		Without PET	With operating PET	Difference
B$_1$ field map *	Magnitude (flip angle α°)	88.9±6.4	61.7±1.8	−3.2±0.7 dB (−30.6±7.8%) attenuation
	Homogeneity (%)	86.7±2.9	79.5±5.2	(−8.4±6.8%) attenuation
MR image **	Transmit Gain (GRE)	+13.4 dB	+16.4 dB	−3 dB attenuation

*
B$_1$ field map: Auto pre-scan off when operating with PET

**
MR image: Auto pre-scan on when operating with PET

TABLE III

MR Image Results Using Body Coil as TX/RX Coil

			Without PET	With operating PET	Difference
MR Image *	Homogeneity (%)	GRE	84.3±4.2	78.8±6.6	−6.6±9.3%
		FSE	80.1±6.5	69.6±6.4	−13.1±11.5%
	SNR	GRE	57.5±3.1	38.7±3.3	−3.5±0.9 dBy (−32.8±8.0%) attenuation
		FSE	37.2±2.3	22.6±1.2	−4.3±0.7 dB (−39.1±7.4%) attenuation

*
MR image: Auto pre-scan on when operating with PET